AIAA JOURNAL
Vol. 50, No. 12, December 2012

Computational Investigation of a Doubly Hinged Flapping-Wing Model

Yunfei Zhang* and Zhengyin Ye†
National Key Laboratory of Science and Technology on Aerodynamic Design and Research, Northwestern Polytechnical University, 710072 Xi'an, People's Republic of China
and
Fei Xie‡
Sichuan Academy of Aerospace Technology, 610100 Chengdu, People's Republic of China

DOI: 10.2514/1.J051108

To understand the effect of the spanning motion of bird wings, a numerical study of a patented model was carried out. A doubly hinged flapping-wing model with the elastic membranes fixed on the upper and lower surfaces is presented. The effect of the membranes is the same as a torsional spring with piecewise stiffness characteristic. The inner wing is driven by harmonic kinematics, while the outer wing responds passively to the aerodynamic and inertial/elastic forces. The ratio of the elastic constant of the lower membrane to the upper one is determined to be a key parameter. Different elastic ratios and hinge-axis positions were considered. It is found that when the elastic ratio is greater than unity, the doubly-hinged model could increase the average lift coefficient compared with the rigid model. On one hand, the average lift coefficient increases with the elastic ratio, but the rate of increase tends to zero. On the other hand, the average drag coefficient first decreases and then increases with the ratio increasing. When the hinge axis moves from wing tip to the root, the average lift coefficient first increases and then decreases, whereas the average drag coefficient behaves in an opposite way.

Nomenclature

$\boldsymbol{A}, \boldsymbol{B}, \boldsymbol{C}$	=	flux Jacobians
$\bar{\boldsymbol{A}}, \bar{\boldsymbol{B}}, \bar{\boldsymbol{C}}$	=	modified flux Jacobians
c	=	chord length of the wing root, m
E	=	specific total internal energy
$\boldsymbol{E}, \boldsymbol{F}, \boldsymbol{G}$	=	inviscid flux vectors
$\boldsymbol{E}_v, \boldsymbol{F}_v, \boldsymbol{G}_v$	=	viscous flux vectors
$\boldsymbol{F}_{\text{air}}$	=	air force acted on the infinitesimal surface element of the outer wing, kg • m/s^2
f	=	frequency, Hz
$\boldsymbol{G}$	=	gravitational force on the outer wing, kg • m/s^2
$\boldsymbol{i}$	=	unit vector along axis x
J_{BD}	=	moment of inertia of the outer wing about axis BD, kg • m/s^2
k_1, k_2	=	elastic constant on the upper and lower surface, N • m
$\boldsymbol{L}_B$	=	angular momentum of the outer wing about point B, kg • m^2/s
$\boldsymbol{L}_B^r$	=	angular momentum of the outer wing about point B in the translating coordinate system moving with B, kg • m^2/s
L_{BD}^r	=	angular momentum of the outer wing about axis BD in the translating coordinate system moving with B, kg • m^2/s
l'_{BE}, l'_{AB}	=	nondimensional length of BE and AB, respectively
M	=	Mach number
M_{air}	=	moment of the air forces on the outer wing about axis BD, kg • m^2/s
M_E	=	moment of the elastic forces about axis BD, kg • m^2/s^2
M_G	=	moment of the gravity of the outer wing about axis BD, kg • m^2/s^2
M_{α_1}	=	acceleration part of the moment of the inertial force about axis BD, kg • m^2/s^2
M_{ω_1}	=	velocity part of the moment of the inertial force about axis BD, kg • m^2/s^2
m	=	mass of an arbitrary particle, kg
m_R	=	mass of the outer wing, kg
$\boldsymbol{n}$	=	unit vector normal to the surface of the control cell; $(n_x, n_y, n_z)T$
Re	=	Reynolds number based on the wing root chord; $\rho_\infty V_\infty c/\mu_\infty$
$\boldsymbol{r}$	=	vector from point B to an arbitrary point on the outer wing surface, m
T	=	period of flapping motion, s
t	=	time, s
$\boldsymbol{U}$	=	vector of conservative variables
u, v, w	=	components of velocity in the x, y, and z Cartesian directions, respectively, m/s
$\boldsymbol{V}$	=	absolute velocity of an arbitrary particle, m/s
$\boldsymbol{V}_B$	=	velocity of point B, m/s
$\boldsymbol{V}_{Cr}$	=	relative velocity of point C with respect to point B, m/s
$\boldsymbol{V}_r$	=	relative velocity of an arbitrary particle with respect to point B, m/s
V_∞	=	freestream velocity, m/s
$\boldsymbol{W}$	=	vector of primitive variables
$\alpha, \alpha_{\text{av}}, \alpha_{\max}$	=	instantaneous, average, and amplitude of pitching angle, respectively
$\boldsymbol{\alpha}_1, \boldsymbol{\alpha}_2$	=	angular acceleration of the inner wing and the outer wing, respectively, m/s^2
α_1, α_2	=	magnitude of the angular acceleration of the inner wing and the outer wing along x direction, respectively, m/s^2
Γ	=	preconditioning matrix
Δ_ξ, ∇_ξ	=	forward and backward difference operators in the ξ direction, respectively
$\varepsilon^{(2)}, \varepsilon^{(4)}$	=	coefficients for artificial diffusion

Received 1 December 2010; revision received 21 December 2011; accepted for publication 21 December 2011.

*Graduate Student, 114 mail box; shanzhongke.zyf@163.com.
†Professor; yezy@nwpu.edu.cn. Member AIAA.
‡Doctor, Hangtian Northern Street, Longquanyi; aeroaero@126.com.

θ_{av} = average flapping angle of the inner wing
θ_{max} = amplitude of the flapping angle of the inner wing
θ_1, θ_2 = instantaneous flapping angle of the inner wing and outer wing, respectively
κ = reduced frequency; $\pi f c/V_\infty$
λ = variable scaling factor
$\lambda_{\bar{A}}$ = eigenvalue of $\bar{\boldsymbol{A}}$
μ_∞ = viscosity coefficient of the freestream, kg/(m • s)
ξ, η, ζ = i, j, k directions, respectively
ρ = air density, kg/m^3
$\boldsymbol{\rho}$ = vector from point B to an arbitrary particle in the outer wing, m
$\boldsymbol{\rho}_{AB}$ = vector from A to B, m
$\boldsymbol{\rho}_{BC}$ = vector from B to C, m
$\sum \boldsymbol{M}_B(\boldsymbol{F}^{(e)})$ = vector summation of moments of all the external forces exerted on the outer wing about point B, kg • m^2/s^2
$\sum M_{BD}(\boldsymbol{F}^{(e)})$ = summation of moments of all the external forces exerted on the outer wing about axis BD, kg • m^2/s^2
τ = pseudo time
φ = phase angle of the flapping angle of the inner wing
Ω = surface of the outer wing
$\Omega_{i,j,k}$ = volume of i, j, k cell
$\boldsymbol{\omega}_1$, $\boldsymbol{\omega}_2$ = angular velocity of the inner wing and outer wing, respectively, m/s
ω_1, ω_2 = angular velocity of the inner wing and outer wing along x direction, respectively, m/s

Subscript

$\bullet_\infty$ = freestream values

Superscript

$\bullet'$ = nondimensional values

I. Introduction

RECENTLY, micro-air vehicles (MAVs) have generated and received considerable attention. The aerodynamics of MAV flight is affected by the scaling of the Reynolds number (the ratio of inertial to viscous force). At low Reynolds number, birds, bats, and insects exhibit desirable performance. Thus, there is an increased need to understand the flapping-wing mechanism in nature, and then to apply it for the design of flapping-wing vehicles.

A good review on this subject was given by Shyy et al. [1]. As for studies of the aeroelasticity of a flexible flapping wing, Liu and Bose [2] investigated the effect of spanwise flexibility on the flukes of an immature fin whale using inviscid computations. They showed that the phase of the flexing motion relative to the heave played a key role in determining thrust and efficiency characteristics of the fin. Zhu [3] researched the effects of chord- and spanwise flexibility of flapping wings. His results suggested that when the wing was immersed in air, the spanwise flexibility (through equivalent plunge and pitch flexibility) increased the thrust without any efficiency reduction within a small range of structural parameters. However, for a wing immersed in water, the spanwise flexibility reduced both the thrust and the efficiency. Heathcote et al. [4] conducted water-tunnel studies to study the effect of spanwise flexibility on the thrust and propulsive efficiency of a plunging flexible wing configuration in forward flight. A degree of spanwise flexibility was found to yield a small increase in the thrust coefficient and a small decrease in power-input requirement, resulting in higher efficiency. But introducing a far greater degree of spanwise flexibility, however, was found to be detrimental. In a subsequent effort, Chimakurthi et al. [5] and Aono et al. [6] conducted computations on the experimental wing configurations of Heathcote et al. [4] using an aeroelastic framework.

Biological observations demonstrate that, with the exception of hummingbirds [7–9], the wing beating of birds consists of four fundamental motions: 1) a plunge motion about the wing root called flapping, 2) a twisting motion of the wing pitch called feathering, 3) the inward folding of the outer wing segment called spanning, and 4) an in-plane motion called lead–lag or simply lagging [9,10]. The spanning motion [11,12] of bird wings is that the wing is spread during the downstroke of the wing, and the outer wing deflects downward during the upstroke of the wing. Based on this spanning motion, Azuma [9] and Sato [13] simplified the spanning motion of bird wings as the doubly hinged wing model. Notably, Toomey and Eldredge [14] and Vanella et al. [15] studied similar two-link models, but their contents were about the chordwise flexibility of two-dimensional insect model.

The wing motions in flapping flight invite an interesting engineering problem: how should the spanning motion be implemented in MAV designs? Ye et al. [16] presented a doubly hinged, passive spanning model in their patent using elastic and inelastic membranes to produce a piecewise torsional stiffness about the outboard hinge. The elastic membrane is affixed to the upper surface of the wing, whereas on the lower surface the inelastic membrane is affixed. Thus, when the wing flaps upward, the outer wing deflects downward because of the fluid dynamic and the inertial/elastic forces; while the wing flaps downward, the wing is spread. In the opinion of Ye et al., the main function of the spanning motion of a bird wing is to increase the average lift coefficient. But what is the aerodynamic performance of the model? What is the main effect of the spanning motion of the flapping wing? When does the doubly hinged wing have better performance than a rigid wing? The present study attempts to address these problems through computational investigations. Because the model of Ye et al. is hard to program, especially when the outer wing is spread, the procedure is hard to converge, and so the model of Ye et al. [16] is modified as follows. The inelastic membrane is replaced by an elastic membrane with a greater elastic constant than that on the upper surface. In this paper, the kinematics of the modified doubly hinged wing model is established, and then the unsteady movement is simulated by a Navier–Stokes (N–S) solver coupled to the wing dynamics. Different elastic ratios of the membranes and different hinge-axis positions are considered. The resulting forces and deflections are presented. It is hoped that the present results are meaningful for flapping MAV design.

II. Numerical Method

A. N–S Solver

The unsteady N–S equations are solved to determine the aerodynamics of the flapping wings. The nondimensional governing equations are as follows [17]:

$$\frac{\partial \boldsymbol{U}}{\partial t}+\frac{\partial \boldsymbol{E}}{\partial x}+\frac{\partial \boldsymbol{F}}{\partial y}+\frac{\partial \boldsymbol{G}}{\partial z}=\frac{1}{Re}\left(\frac{\partial \boldsymbol{E}_v}{\partial x}+\frac{\partial \boldsymbol{F}_v}{\partial y}+\frac{\partial \boldsymbol{G}_v}{\partial z}\right) \quad (1)$$

$\boldsymbol{U}$ is $(\rho, \rho u, \rho v, \rho w, \rho E)^T$. The freestream velocity V_∞, the chord length c of the wing root, and the ratio of chord length to the freestream velocity c/V_∞ are used as the velocity, length, and time scales.

Time-derivative preconditioning [18–20] is incorporated to alleviate the stiffness and associated convergence problems that occur at low Mach numbers. The preconditioning is applied with a dual-time step approach [21–23], in which a pseudo time derivative is added to the governing equations. The governing equations [Eq. (1)] then become

$$\Gamma\frac{\partial \boldsymbol{W}}{\partial \tau}+\frac{\partial \boldsymbol{U}}{\partial t}+\frac{\partial \boldsymbol{E}}{\partial x}+\frac{\partial \boldsymbol{F}}{\partial y}+\frac{\partial \boldsymbol{G}}{\partial z}=\frac{1}{Re}\left(\frac{\partial \boldsymbol{E}_v}{\partial x}+\frac{\partial \boldsymbol{F}_v}{\partial y}+\frac{\partial \boldsymbol{G}_v}{\partial z}\right) \quad (2)$$

in which $\boldsymbol{W}=(p,u,v,w,T)^T$. The preconditioning matrix used here is developed by Pletcher and Chen [18].

The governing equations are discretized in a finite volume framework [24–26]. The structured grid is developed in C-topology

by transfinite interpolation method. The solution variables are stored at the cell centers. Applying Eq. (2) to each cell separately

$$\Gamma \frac{\mathrm{d}}{\mathrm{d}\tau}(\Omega_{i,j,k}\boldsymbol{W}_{i,j,k}) + \frac{\mathrm{d}}{\mathrm{d}t}(\Omega_{i,j,k}\boldsymbol{U}_{i,j,k}) + \ell \boldsymbol{U}_{i,j,k} = 0 \tag{3}$$

in which ℓ is a spatial discretization operator defined by $\ell = \ell_C + \ell_D + \ell_{AD}$, with the subscripts C, D, and AD referring to convection, diffusion, and artificial dissipation, respectively. The convective fluxes at the cell faces are obtained by an averaging process. The artificial dissipation is based on the model introduced by Jameson et al. [24]. The preconditioning matrix is included in the dissipation flux [19]:

$$\ell_C \boldsymbol{U}_{i,j,k} = \sum_{l=1}^{6}(\boldsymbol{E}n_x + \boldsymbol{F}n_y + \boldsymbol{G}n_z)\Delta S_l$$

$$\ell_D \boldsymbol{U}_{i,j,k} = -\frac{1}{Re}\sum_{l=1}^{6}(\boldsymbol{E}_{\boldsymbol{v}}n_x + \boldsymbol{F}_{\boldsymbol{v}}n_y + \boldsymbol{G}_{\boldsymbol{v}}n_z)\Delta S_l$$

$$\ell_{AD}\boldsymbol{U}_{i,j,k} = -(D_\xi^2 - D_\xi^4 + D_\eta^2 - D_\eta^4 + D_\zeta^2 - D_\zeta^4)\boldsymbol{U}_{i,j,k}$$

$$D_\xi^2 \boldsymbol{U}_{i,j,k} = \nabla_\xi[(\Gamma_{i+1/2,j,k}\lambda_{i+1/2,j,k}\varepsilon^{(2)}_{i+1/2,j,k})\Delta_\xi]\boldsymbol{U}_{i,j,k}$$

$$D_\xi^4 \boldsymbol{U}_{i,j,k} = \nabla_\xi[(\Gamma_{i+1/2,j,k}\lambda_{i+1/2,j,k}\varepsilon^{(4)}_{i+1/2,j,k})\Delta_\xi\nabla_\xi\Delta_\xi]\boldsymbol{U}_{i,j,k}$$

in which $\boldsymbol{n} = (n_x, n_y, n_z)^T$ is the unit vector normal to the surface of the control cell. The detailed definition for $\varepsilon^{(2)}$ and $\varepsilon^{(4)}$ can be found in [26].

The implicit lower–upper symmetric Gauss–Seidel scheme [27–29] coupling with an implicit residual smoothing is used for the time integration to achieve faster convergence of the proposed numerical method. The pseudo time derivative is discretized with a Euler backward difference, and the physical time derivative is discretized with a three-point backward difference, yielding

$$\Gamma^m \Omega^{n+1}_{i,j,k}\frac{\Delta \boldsymbol{W}^m_{i,j,k}}{\Delta\tau} + \frac{3\Omega^{n+1}_{i,j,k}\boldsymbol{U}^{m+1}_{i,j,k} - 4\Omega^{n}_{i,j,k}\boldsymbol{U}^{n}_{i,j,k} + \Omega^{n-1}_{i,j,k}\boldsymbol{U}^{n-1}_{i,j,k}}{2\Delta t} + \ell_C \boldsymbol{U}^{m+1}_{i,j,k} = -(\ell_D \boldsymbol{U}^m_{i,j,k} + \ell_{AD}\boldsymbol{U}^m_{i,j,k}) \tag{4}$$

in which $\Delta \boldsymbol{W}^m_{i,j,k} = \boldsymbol{W}^{m+1}_{i,j,k} - \boldsymbol{W}^m_{i,j,k}$, the superscript m is the pseudosubiteration counter, and n is the physical time counter. The inviscid flux vectors are linearized about pseudo time level m as

$$\ell_C \boldsymbol{U}^{m+1}_{i,j,k} = \ell_C \boldsymbol{U}^m_{i,j,k} + \left(\frac{\partial \ell_C \boldsymbol{U}_{i,j,k}}{\partial \boldsymbol{W}}\frac{\partial \boldsymbol{W}}{\partial t}\right)^m \Delta t = \ell_C \boldsymbol{U}^m_{i,j,k} + \sum_{l=1}^{6}\left[\left(\frac{\partial \boldsymbol{E}}{\partial \boldsymbol{W}}n_x + \frac{\partial \boldsymbol{F}}{\partial \boldsymbol{W}}n_y + \frac{\partial \boldsymbol{G}}{\partial \boldsymbol{W}}n_z\right)\Delta S_l\right]^m \Delta \boldsymbol{W}^m_{i,j,k} \tag{5}$$

Let $l = 1$–6 denote $(i-1/2, j, k)$, $(i, j-1/2, k)$, $(i, j, k$–$1/2)$, $(i+1/2, j, k)$, $(i, j+1/2, k)$, and $(i, j, k+1/2)$, respectively. Let

$$\boldsymbol{A} = \left[\left(\frac{\partial \boldsymbol{E}}{\partial \boldsymbol{W}}n_x + \frac{\partial \boldsymbol{F}}{\partial \boldsymbol{W}}n_y + \frac{\partial \boldsymbol{G}}{\partial \boldsymbol{W}}n_z\right)\Delta S_l\right]_{l=1,4},$$

$$\boldsymbol{B} = \left[\left(\frac{\partial \boldsymbol{E}}{\partial \boldsymbol{W}}n_x + \frac{\partial \boldsymbol{F}}{\partial \boldsymbol{W}}n_y + \frac{\partial \boldsymbol{G}}{\partial \boldsymbol{W}}n_z\right)\Delta S_l\right]_{l=2,5}, \quad \text{and}$$

$$\boldsymbol{C} = \left[\left(\frac{\partial \boldsymbol{E}}{\partial \boldsymbol{W}}n_x + \frac{\partial \boldsymbol{F}}{\partial \boldsymbol{W}}n_y + \frac{\partial \boldsymbol{G}}{\partial \boldsymbol{W}}n_z\right)\Delta S_l\right]_{l=3,6}$$

Substituting Eq. (5) into Eq. (4), yielding

$$\begin{aligned}
&\Omega^{n+1}_{i,j,k}\left(\frac{\Gamma^m}{\Delta\tau} + \frac{3\boldsymbol{T}^m}{2\Delta t}\right)\Delta \boldsymbol{W}^m_{i,j,k} + (\boldsymbol{A}\Delta \boldsymbol{W})^m_{i-1/2,j,k} + (\boldsymbol{A}\Delta \boldsymbol{W})^m_{i+1/2,j,k} \\
&\quad + (\boldsymbol{B}\Delta \boldsymbol{W})^m_{i,j-1/2,k} + (\boldsymbol{B}\Delta \boldsymbol{W})^m_{i,j+1/2,k} + (\boldsymbol{C}\Delta \boldsymbol{W})^m_{i,j,k-1/2} \\
&\quad + (\boldsymbol{C}\Delta \boldsymbol{W})^m_{i,j,k+1/2} = -\boldsymbol{P}^m_{i,j,k} \\
&\boldsymbol{P}^m_{i,j,k} = \frac{3\Omega^{n+1}_{i,j,k}\boldsymbol{U}^m_{i,j,k} - 4\Omega^{n}_{i,j,k}\boldsymbol{U}^{n}_{i,j,k} + \Omega^{n-1}_{i,j,k}\boldsymbol{U}^{n-1}_{i,j,k}}{2\Delta t} \\
&\quad + (\ell_C \boldsymbol{U}^m_{i,j,k} + \ell_D \boldsymbol{U}^m_{i,j,k} + \ell_{\mathrm{AD}}\boldsymbol{U}^m_{i,j,k})
\end{aligned} \tag{6}$$

The flux Jacobians are modified because of the preconditioning of the equations:

$$\bar{\boldsymbol{A}} = \Gamma^{-1}\boldsymbol{A}, \qquad \bar{\boldsymbol{A}} = \bar{\boldsymbol{A}}^+ + \bar{\boldsymbol{A}}^-, \qquad \bar{\boldsymbol{A}}^\pm = \frac{\bar{\boldsymbol{A}} \pm \chi\sigma_{\bar{\boldsymbol{A}}}\boldsymbol{I}}{2},$$

$$\Gamma\bar{\boldsymbol{A}}^\pm = \frac{\Gamma\bar{\boldsymbol{A}} \pm \chi\sigma_{\bar{\boldsymbol{A}}}\Gamma}{2} = \frac{\boldsymbol{A} \pm \chi\sigma_{\bar{\boldsymbol{A}}}\Gamma}{2}$$

in which $\chi = 1.01$, $\sigma_{\bar{\boldsymbol{A}}} = \max(|\lambda_{\bar{\boldsymbol{A}}}|)$. The contribution of the inviscid fluxes at each cell face is

$$(\Gamma\bar{\boldsymbol{A}}\Delta \boldsymbol{W})^m_{i-1/2,j,k} = \Gamma\bar{\boldsymbol{A}}^+_{i-1/2,j,k}\Delta \boldsymbol{W}^m_{i,j,k} + \Gamma\bar{\boldsymbol{A}}^-_{i-1/2,j,k}\Delta \boldsymbol{W}^m_{i-1,j,k}$$

$$(\Gamma\bar{\boldsymbol{A}}\Delta \boldsymbol{W})^m_{i+1/2,j,k} = \Gamma\bar{\boldsymbol{A}}^+_{i+1/2,j,k}\Delta \boldsymbol{W}^m_{i,j,k} + \Gamma\bar{\boldsymbol{A}}^-_{i+1/2,j,k}\Delta \boldsymbol{W}^m_{i+1,j,k}$$

Define quantities related to $\boldsymbol{B}$ and $\boldsymbol{C}$ in the same way. When $\Delta\tau \to \infty$, Eq. (6) can be written as

$$\begin{aligned}
&(L + D + U)\Delta \boldsymbol{W}^m_{i,j,k} = -\alpha\Gamma^{-1,m}\boldsymbol{P}^m_{i,j,k} \\
&L = \alpha\Gamma^{-1,m}(\Gamma\bar{\boldsymbol{A}}^-_{i-1,j,k} + \Gamma\bar{\boldsymbol{B}}^-_{i,j-1,k} + \Gamma\bar{\boldsymbol{C}}^-_{i,j,k-1}) \\
&D = \Gamma^{-1,m}\boldsymbol{T}^m + \frac{\alpha\chi}{2}(\sigma_{\bar{\boldsymbol{A}}_1} + \sigma_{\bar{\boldsymbol{B}}_2} + \sigma_{\bar{\boldsymbol{C}}_3} + \sigma_{\bar{\boldsymbol{A}}_4} + \sigma_{\bar{\boldsymbol{B}}_5} + \sigma_{\bar{\boldsymbol{C}}_6}) \\
&U = \alpha\Gamma^{-1,m}(\Gamma\bar{\boldsymbol{A}}^-_{i+1,j,k} + \Gamma\bar{\boldsymbol{B}}^-_{i,j+1,k} + \Gamma\bar{\boldsymbol{C}}^-_{i,j,k+1})
\end{aligned} \tag{7}$$

Equation (7) can be approximately factored as

$$(L + D)D^{-1}(D + U)\Delta \boldsymbol{W}^m_{i,j,k} = -\alpha\Gamma^{-1,m}\boldsymbol{P}^m_{i,j,k} \tag{8}$$

No-slip condition is employed on the wing surface, and nonreflecting boundary condition based on Riemann invariants is employed on the far field. The boundary conditions should also be modified as referenced in [20]. Menter's shear stress transport turbulent model [30,31] is applied for calculating the turbulence flows at low Reynolds numbers.

B. N–S Code Validation

In 1987, Koochesfahani [32] performed experiments in the low-speed water channel of the Graduate Aeronautical Laboratories of the California Institute of Technology. The vortical flow patterns in the wake of a NACA 0012 airfoil pitching at small amplitudes about the one-fourth-chord point at pitching frequency f. The airfoil had a chord of 0.08 m and a span of 0.39 m. The freestream velocity was approximately 0.15 m/s, resulting in a chord Reynolds number of 12,000. The pitching mode was given by $\alpha = \alpha_{\mathrm{av}} + \alpha_{\max}\sin(2\kappa t)$, $\alpha_{\mathrm{av}} = 0.0$.

The results of Koochesfahani are used to validate the N–S solver. The C-grid is used with 290×70 grids to compute the thrust curves. About five pitching cycles are carried out to get the periodic thrust curve. Figure 1 compares the present computational results with existing experimental [32] and computational [33,34] data. The same trend is observed between the experimental and N–S predictions for the thrust coefficient. To obtain the vortex structure behind the airfoil, the grid number is increased to 1000×180. Figure 2 shows the comparison of experimental and numerical wake vortex structure, noting a close similarity with the experimental visualization.

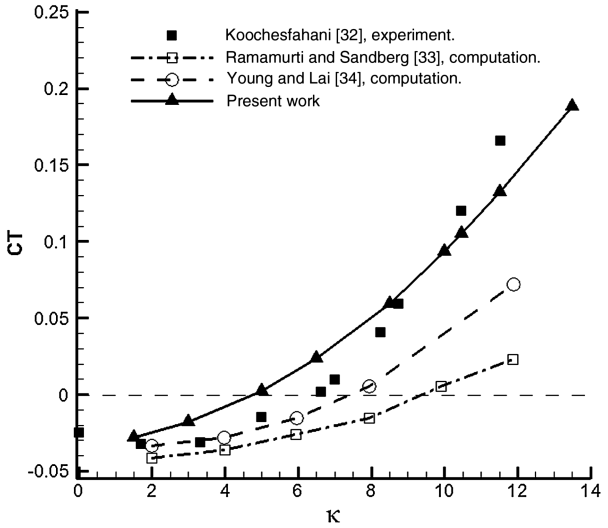

Fig. 1 Comparison of N–S simulations to experimental [32] and computational [33,34] data, $\alpha_{\max} = 2$ deg.

III. Kinematics of the Flapping Wing

To investigate the spanwise deflection motion of bird wings, the flapping kinematics was established based on the patent of Ye et al. [16]. This flapping model takes only the flapping and spanning motions into account. The model reduces the bird's spanning motion to the folding of rigid segments. As shown in Fig. 3a, *ABDH* denotes the inner wing, and *BEID* is the outer wing. The elastic membranes are fixed on the upper and lower surfaces of the inner wing and outer wing, with the elastic constants being k_1 and k_2, respectively. *BD* is the hinge axis connecting the inner wing and the outer wing. The inner wing is driven harmonically while the outer wing responds passively to fluid dynamic, gravitational, and the inertial/elastic forces. *C* is the center of mass of the outer wing. *F* is the projection of *C* on the *y*-*z* plane. As shown in Fig. 3b, the flapping angle of the inner wing is $\theta_1 = \theta_{\text{av}} + \theta_{\max}\sin(2\kappa t + \varphi)$, which is positive when measured counterclockwise (looking along the positive *x* axis) from the *y* axis to the direction of the inner wing. Both θ_1 and θ_2 are positive counterclockwise (looking along the positive *x* axis).

The angular momentum of the outer wing about point *B* is

$$\boldsymbol{L}_B = \sum \boldsymbol{\rho} \times m\boldsymbol{V} = \sum \boldsymbol{\rho} \times m(\boldsymbol{V}_B + \boldsymbol{V}_r) = \sum \boldsymbol{\rho} \times m\boldsymbol{V}_B + \sum \boldsymbol{\rho} \times m\boldsymbol{V}_r = m_R \boldsymbol{\rho}_{BC} \times \boldsymbol{V}_B + \boldsymbol{L}_B^r \tag{9}$$

in which $\sum$ denotes the summation of the expression after the symbol for all the particles in the outer wing.

However

$$\frac{\mathrm{d}\boldsymbol{\rho}_{BC}}{\mathrm{d}t} = \frac{\mathrm{d}}{\mathrm{d}t}(\boldsymbol{\rho}_{AC} - \boldsymbol{\rho}_{AB}) = \boldsymbol{V}_C - \boldsymbol{V}_B = \boldsymbol{V}_{Cr}, \qquad \boldsymbol{V}_B = \boldsymbol{\omega}_1 \times \boldsymbol{\rho}_{AB}$$

And so Eq. (10) is obtained by differentiation:

$$\frac{\mathrm{d}\boldsymbol{L}_B}{\mathrm{d}t} = m_R \frac{\mathrm{d}\boldsymbol{\rho}_{BC}}{\mathrm{d}t} \times \boldsymbol{V}_B + m_R \boldsymbol{\rho}_{BC} \times \frac{\mathrm{d}\boldsymbol{V}_B}{\mathrm{d}t} + \frac{\mathrm{d}\boldsymbol{L}_B^r}{\mathrm{d}t} = m_R \boldsymbol{V}_{Cr} \times \boldsymbol{V}_B + m_R \boldsymbol{\rho}_{BC} \times (\boldsymbol{\alpha}_1 \times \boldsymbol{\rho}_{AB} + \boldsymbol{\omega}_1 \times \boldsymbol{V}_B) + \frac{\mathrm{d}\boldsymbol{L}_B^r}{\mathrm{d}t} \tag{10}$$

Apply the theorem of angular momentum of particle system about an arbitrary point to the outer wing [35]

$$\frac{\mathrm{d}\boldsymbol{L}_B}{\mathrm{d}t} = \sum \boldsymbol{M}_B(\boldsymbol{F}^{(e)}) - \boldsymbol{V}_B \times m_R \boldsymbol{V}_C \tag{11}$$

Thus

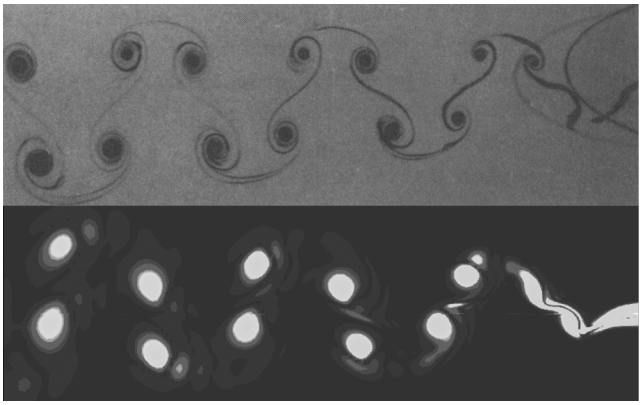

a) $\alpha_{max} = 4°$, $\kappa = 3.0895$

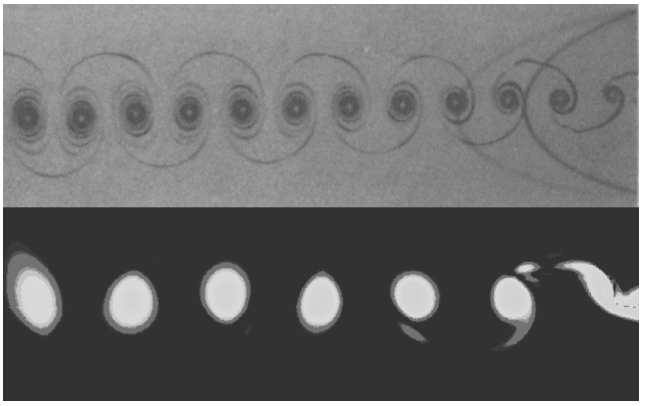

b) $\alpha_{max} = 2°$, $\kappa = 6.68$

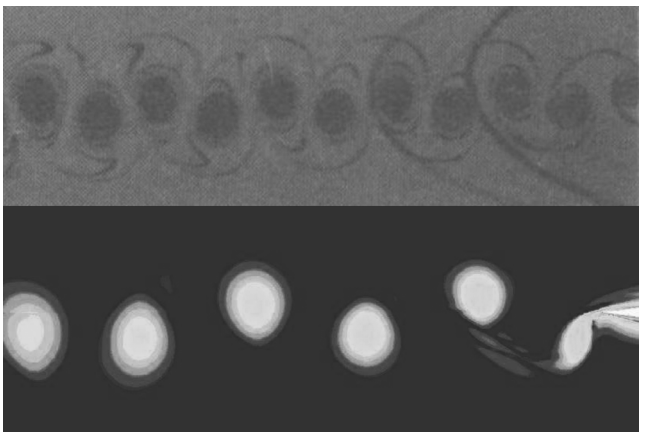

c) $\alpha_{max} = 2°$, $\kappa = 10.02$

Fig. 2 Wake comparison of experiment 32 (upper) and present computations (lower). Flow is from right to left.

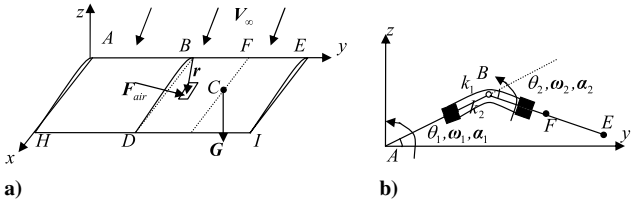

a) b)

Fig. 3 Schematic diagrams of the flapping wing with spanwise deflection motion. b) is the side view of a).

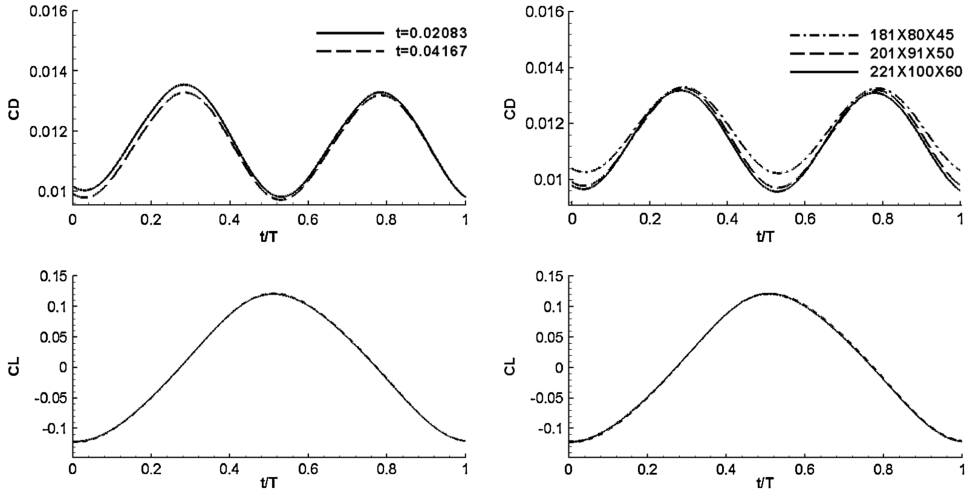

Fig. 4 Convergence study of time step (left) and grid resolution (right).

$$m_R \boldsymbol{V}_{Cr} \times \boldsymbol{V}_B + m_R \boldsymbol{\rho}_{BC} \times (\boldsymbol{\alpha}_1 \times \boldsymbol{\rho}_{AB} + \boldsymbol{\omega}_1 \times \boldsymbol{V}_B) + \frac{\mathrm{d}\boldsymbol{L}_B^r}{\mathrm{d}t} = \sum \boldsymbol{M}_B(\boldsymbol{F}^{(e)}) - \boldsymbol{V}_B \times m_R \boldsymbol{V}_C \tag{12}$$

However, $m_R \boldsymbol{V}_{Cr} \times \boldsymbol{V}_B = -\boldsymbol{V}_B \times m_R \boldsymbol{V}_C$, hence

$$\begin{aligned}\frac{\mathrm{d}\boldsymbol{L}_B^r}{\mathrm{d}t} &= \sum \boldsymbol{M}_B(\boldsymbol{F}^{(e)}) - m_R \boldsymbol{\rho}_{BC} \times (\boldsymbol{\alpha}_1 \times \boldsymbol{\rho}_{AB} + \boldsymbol{\omega}_1 \times \boldsymbol{V}_B) \\ &= \sum \boldsymbol{M}_B(\boldsymbol{F}^{(e)}) - m_R[(\boldsymbol{\rho}_{BC} \bullet \boldsymbol{\rho}_{AB})\boldsymbol{\alpha}_1 - (\boldsymbol{\rho}_{BC} \bullet \boldsymbol{\alpha}_1)\boldsymbol{\rho}_{AB} \\ &\quad + (\boldsymbol{\rho}_{BC} \bullet \boldsymbol{V}_B)\boldsymbol{\omega}_1 - (\boldsymbol{\rho}_{BC} \bullet \boldsymbol{\omega}_1)\boldsymbol{V}_B]\end{aligned} \tag{13}$$

The projection of both sides of Eq. (13) on axis BD [i.e., get the dot production of Eq. (13) with the unit vector $\boldsymbol{i}$] is

$$\frac{\mathrm{d}\boldsymbol{L}_{BD}^r}{\mathrm{d}t} = \sum \boldsymbol{M}_{BD}(\boldsymbol{F}^{(e)}) - m_R[(\boldsymbol{\rho}_{BC} \bullet \boldsymbol{\rho}_{AB})\alpha_1 + (\boldsymbol{\rho}_{BC} \bullet \boldsymbol{V}_B)\omega_1] \tag{14}$$

In the translating coordinate system moving with point B, the motion of the outer wing is the rotation about axis BD, and so $L_{BD}^r = J_{BD}(\omega_1 + \omega_2)$. Hence

$$J_{BD}\frac{\mathrm{d}}{\mathrm{d}t}(\omega_1 + \omega_2) = \sum M_{BD}(\boldsymbol{F}^{(e)}) - m_R[(\boldsymbol{\rho}_{BC} \bullet \boldsymbol{\rho}_{AB})\alpha_1 + (\boldsymbol{\rho}_{BC} \bullet \boldsymbol{V}_B)\omega_1] \tag{15}$$

in which $\sum M_{BD}(\boldsymbol{F}^{(e)}) = M_E + (\boldsymbol{\rho}_{BC} \times \boldsymbol{G}) \bullet \boldsymbol{i} + \iint_\Omega (\boldsymbol{r} \times \boldsymbol{F}_{\mathrm{air}}) \bullet \boldsymbol{i}\,\mathrm{d}S$. Hence

$$\begin{aligned}\alpha_2 &= \frac{1}{J_{BD}}\left\{\sum M_{BD}(\boldsymbol{F}^{(e)}) - [m_R(\boldsymbol{\rho}_{BC} \bullet \boldsymbol{\rho}_{AB}) + J_{BD}]\alpha_1 - m_R(\boldsymbol{\rho}_{BC} \bullet \boldsymbol{V}_B)\omega_1\right\} = \frac{1}{J_{BD}}(M_E + M_G + M_{\mathrm{air}} + M_{\alpha_1} + M_{\omega_1}) \\ M_E &= \begin{cases} -k_1\theta_2 & \theta_2 < 0 \\ -k_2\theta_2 & \theta_2 > 0 \end{cases}; \qquad M_G = (\boldsymbol{\rho}_{BC} \times \boldsymbol{G}) \bullet \boldsymbol{i} \\ M_{\mathrm{air}} &= \iint_\Omega (\boldsymbol{r} \times \boldsymbol{F}_{\mathrm{air}}) \bullet \boldsymbol{i}\,\mathrm{d}S \\ M_{\alpha_1} &= -[m_R(\boldsymbol{\rho}_{BC} \bullet \boldsymbol{\rho}_{AB}) + J_{BD}]\alpha_1 \\ M_{\omega_1} &= -m_R(\boldsymbol{\rho}_{BC} \bullet \boldsymbol{V}_B)\omega_1\end{aligned} \tag{16}$$

Selecting c, V_∞, and ρ_∞ as the reference variables, the nondimensional form of Eq. (16) can be obtained as follows:

$$\alpha_2' = \frac{1}{J_{BD}'}(M_E' + M_G' + M_{\mathrm{air}}' + M_{\alpha_1}' + M_{\omega_1}') \tag{17}$$

With the aforementioned description, the fluid dynamics and the structural dynamics are solved independently with the same boundary information (aerodynamic forces and structural displacements). The far-field boundaries are fixed, and the grid is regenerated using transfinite interpolation [36,37] for each time step of the calculation.

IV. Results and Discussion

A. Evaluation of Computational Parameters

Considering the flight condition of a pigeon given in [38], the following parameters are chosen for computation. A rectangular wing with aspect ratio AR = 5 and a NACA 0004 cross section is chosen. Only half of the total wing span is modeled because the symmetry condition can be exploited. The chord of the flapping wing is $c = 0.1$ m. The material of the flapping wing is distributed uniformly, and the density is 120 kg/m^3. Because the density of the material is low, the moment due to gravity on the outer wing about axis BD in Eq. (17) is herein neglected. The elastic constant of the membrane on the upper surface is selected as $k_1 = 0.0064$ Nm. The

Table 1 Hinge-axis position and the corresponding nondimensional parameters

Hinge-axis position [i.e., $l'_{BE}/(l'_{AB} + l'_{BE})$], %	J'_{BD}	m'_R	l'_{AB}	l'_{BF}
32.9	0.49103	2.204082	1.6773	0.4113
43.2	1.112576	2.889796	1.42032	0.53984
52.3	1.969326	3.502041	1.19186	0.654

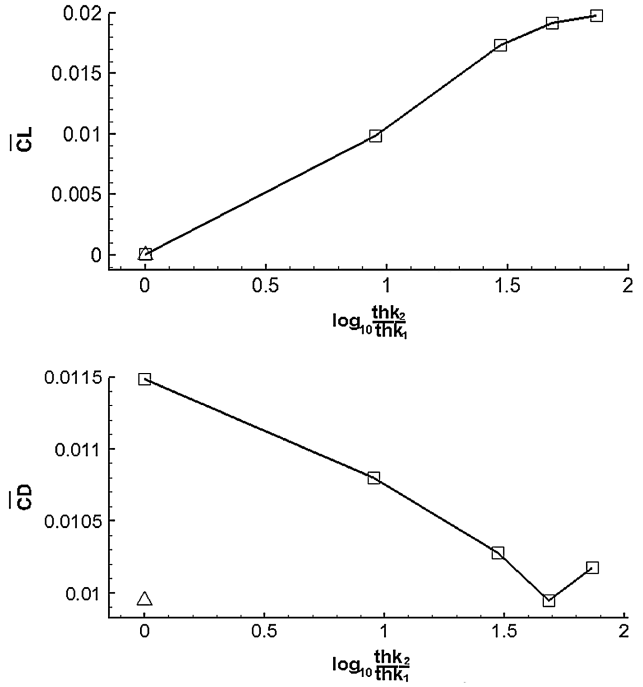

Fig. 5 Average lift and drag coefficients as functions of $\log_{10}\frac{\tanh k_2}{\tanh k_1}$. Rigid wing (triangle); doubly hinged model for $k_1 = 0.0064$ Nm (square).

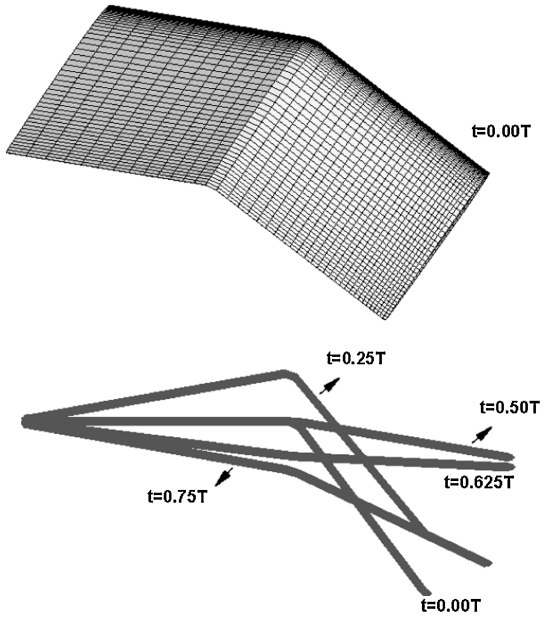

Fig. 6 Wing-surface positions over one flapping cycle, $k_2 = 80k_1$.

density of the material and the elastic constant are determined by the author's unpublished experiment. The computational condition is $M = 0.0294$, $Re = 68,458$, $\theta_{av} = 0$, $\theta_{max} = 10$ deg, $\varphi = 0$, and $\kappa = 0.188495$. Fixing these parameters, the effects of the elastic

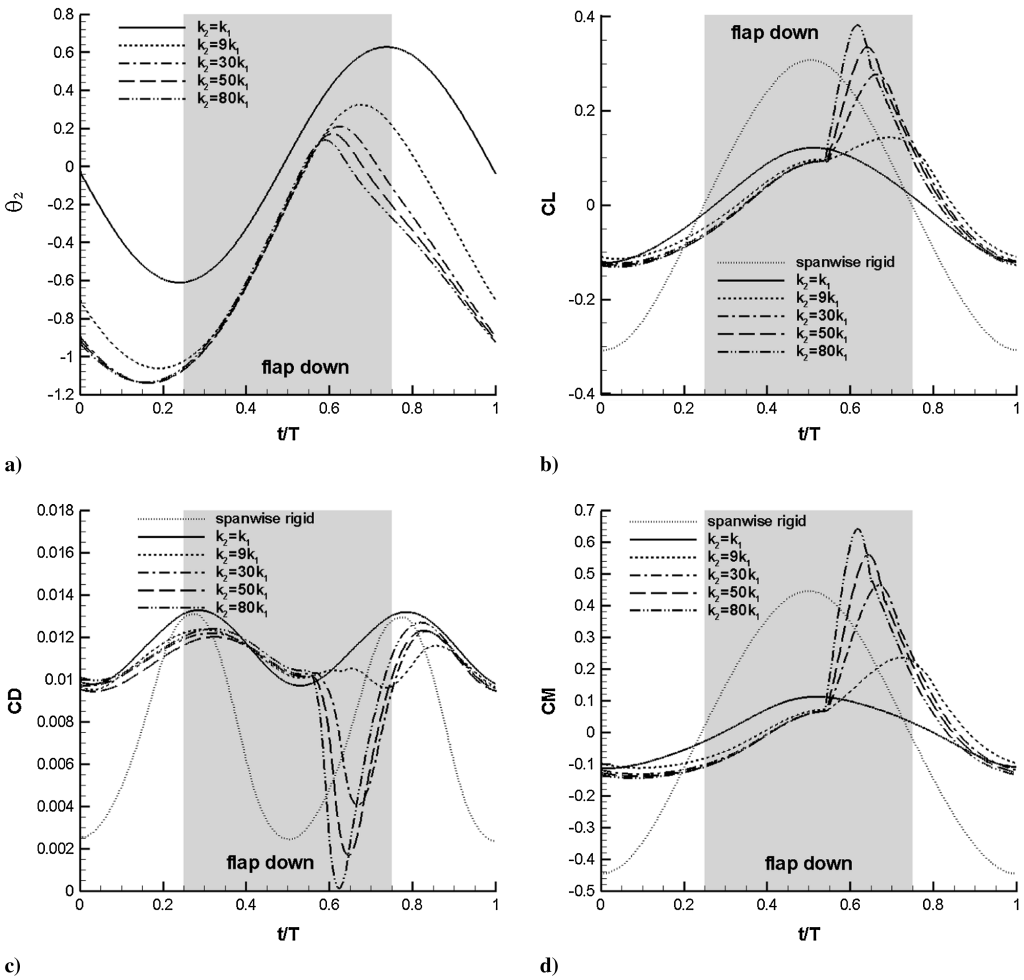

Fig. 7 Comparisons of doubly hinged wing of different elastic constants with rigid wing: a) deflection angle, b), c) and d) are instantaneous lift, drag and bending moment coefficient, respectively.

constant of the membrane on the lower surface and the hinge-axis position are investigated in this paper.

To assess the independence of the numerical solution to grid numbers and time step, a grid convergence and time-step sensitivity study are performed. Two different nondimensional time steps are tested, which were 0.02083 (800 steps per flapping cycle) and 0.04167 (400 steps per flapping cycle). The grid numbers are 181 × 80 × 45 (41 points along wing span, 51 points along wing chord),

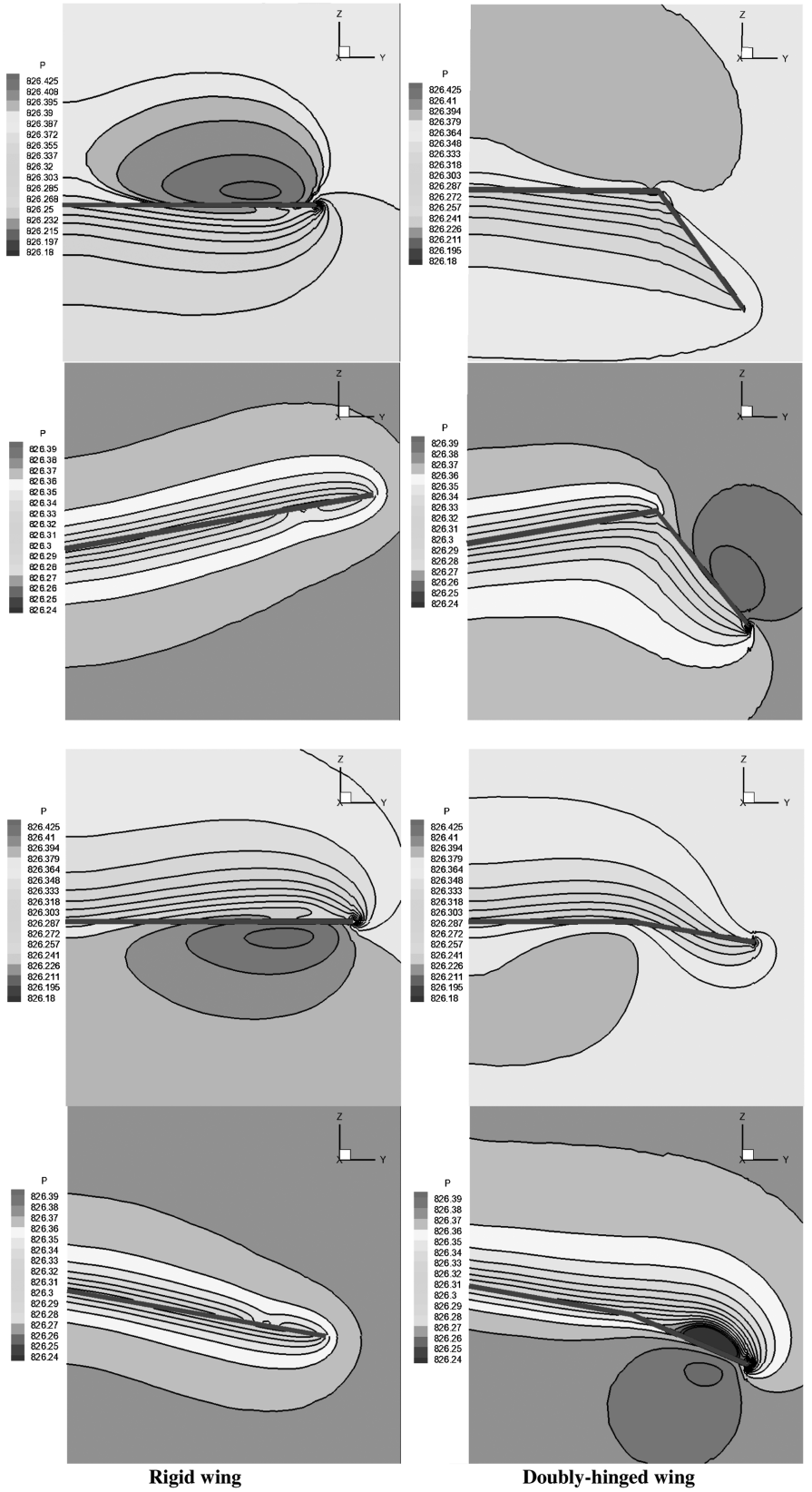

Fig. 8 Pressure contours at four different time instants in a stroke period at 0.25*c* section. The time instants are 0.0*T* (top), 0.25*T*, 0.5*T*, and 0.75*T* (bottom); $k_2 = 50k_1$.

$201 \times 91 \times 50$ (43 points along wing span, 56 points along wing chord), and $221 \times 100 \times 60$ (51 points along wing span, 61 points along wing chord). The computational parameters were the same as mentioned earlier with $k_2 = k_1$. The corresponding lift and drag coefficients are shown in Fig. 4. Based on this analysis, a time step of 0.04167 and a grid of $201 \times 91 \times 50$ are used in all cases discussed as follows. The y^+ distance for these computations is about 5. The outer boundary is $25c$ away from the wing in the spanwise direction and $20c$ in other directions.

B. Effect of Elastic Constant

As shown in Table 1, the hinge-axis position is denoted by $l'_{BE}/(l'_{AB} + l'_{BE}) \times 100\%$, which in this section is 43.2%. The other parameters are found in Table 1. Because the kinematics of the inner wing is harmonic, the wing is symmetrical and M_G is neglected in Eq. (17), when $k_2 = k_1$, the upward and downward deflection motion of the outer wing should be symmetrical. However, if $k_2 > k_1$, then the upward deflection amplitude should be less than the downward deflection amplitude. This anticipated result can be used to check the doubly hinged model in this paper. Hence, by keeping k_1 constant, the aerodynamics for different k_2 is computed in this section.

Figure 5 shows the average lift and drag coefficients as a function of $\log_{10}(\tanh k_2/\tanh k_1)$. The delta symbols in Fig. 5 denote the rigid flapping wing. The square symbols denote the doubly hinged model, and k_2/k_1 has values 1, 9, 30, 50, and 80, respectively. The outer wing of the doubly hinged model in this paper can deflect upward and downward when k_1 and k_2 are finite. But when $k_1 \to \infty$ or $k_2 \to \infty$, the outer wing can only deflect upward or downward. When $k_1 \to \infty$ and $k_2 \to \infty$ at the same time, the doubly hinged wing becomes the rigid wing. As can be seen in Fig. 5, when $\log_{10}(\tanh k_2/\tanh k_1) = 0$ (i.e., $k_2/k_1 = 1$), the average lift coefficient of the doubly hinged wing is zero, as anticipated at the beginning of Sec. IV.B. Compared with the rigid wing, when $\log_{10}(\tanh k_2/\tanh k_1) > 0$ (i.e., $k_2 > k_1$), the doubly hinged wing model can enhance the average lift coefficient, but the average drag coefficient is increased at the same time. The average lift coefficient increases as $\log_{10}(\tanh k_2/\tanh k_1)$ increases. This observation suggests an optimal $\log_{10}(\tanh k_2/\tanh k_1)$ to achieve the best lift-to-drag ratio. Figure 6 shows the surface grid of the flapping wing and the different position of the doubly hinged wing at different time in a flapping cycle. From Fig. 6, an intuition for the doubly hinged wing motion can be developed.

Figure 7a is the deflection angle of the outer wing as a function of time for different elastic constants. This figure shows that when $k_2 = k_1$, the deflection motion is symmetrical as expected. As k_2 increases, the upward deflection amplitude becomes smaller and the time interval becomes shorter during which the outer wing deflects upward. Figures 7b–7d are the instantaneous lift coefficient, drag coefficient, and bending-moment coefficient about the wing root. When $k_2 > k_1$ and the sign of the deflection angle of the outer wing changes from negative to positive around $t/T = 0.55$, the first derivatives of the curves jump sharply. From Eq. (16), it can be found that when the deflection angle of the outer wing changes from negative to positive around $t/T = 0.55$, M_E changes drastically, whereas other moments almost stay the same. This causes α_2 and the angular velocity ω_2 to change drastically, ultimately causing a sharp jump in the first derivatives of the lift, drag, and moment coefficients. During the interval when the outer wing deflects upward around

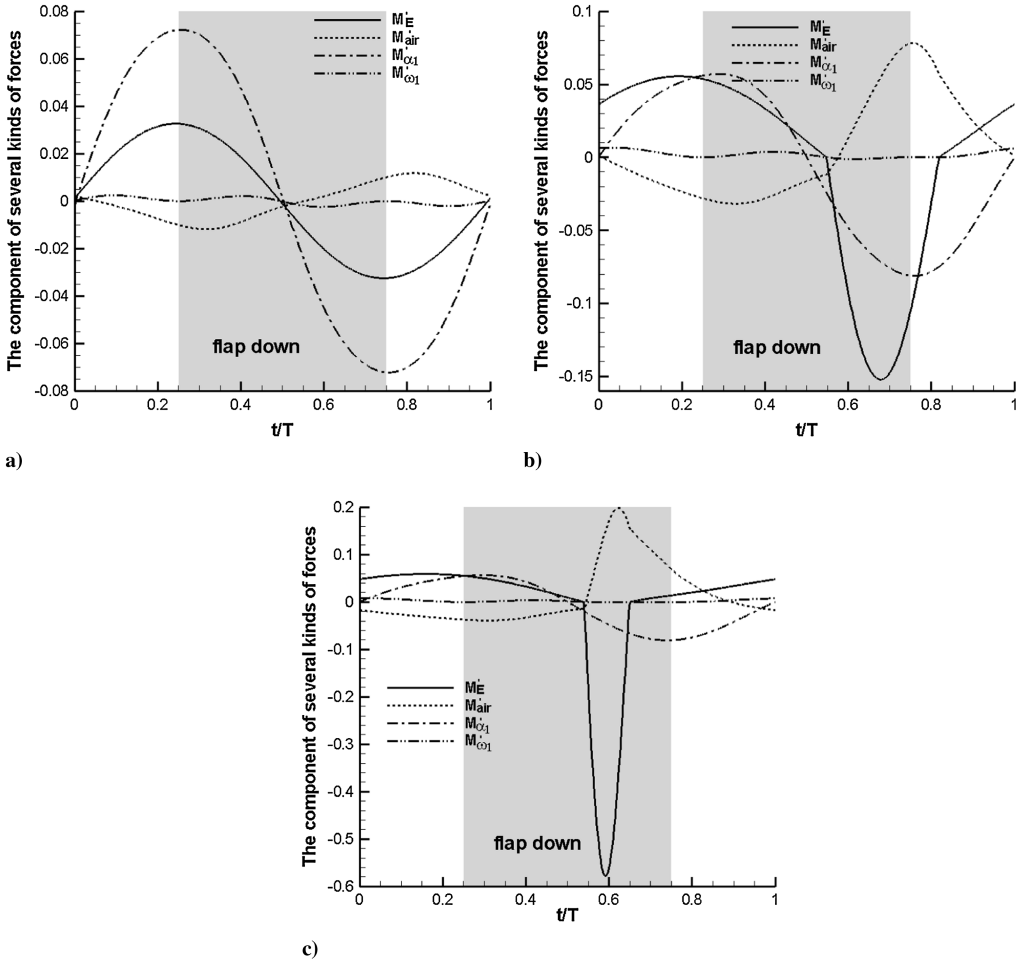

Fig. 9 Comparisons of the moment components in Eq. (17) that determine the angular acceleration of the outer wing: a) $k_2 = k_1$, b) $k_2 = 9k_1$, and c) $k_2 = 80k_1$.

$t/T = 0.55 \sim 0.75$, the curves of the lift coefficient and the bending-moment coefficient exhibit convex peak, whereas the curves of the drag coefficient exhibit concave peak. This is caused by the difference between the elastic constant on the upper surface and that on the lower surface.

As can be seen in Fig. 7b, compared with rigid wing, the doubly hinged wing model can reduce the negative lift remarkably during the upstroke. This effect causes the average lift coefficient of the doubly hinged wing to be greater than the rigid wing when $k_2 > k_1$. It is seen in Fig. 7c that the drag for the rigid wing is smallest at the mid-downstroke around $t/T = 0.5$ and the mid-upstroke around $t/T = 0$ (or 1), but the deflection motion of the outer wing increases the drag of the doubly hinged wing at these intervals. The absolute value of the bending moment about the wing root could be selected as a parameter that scales the instantaneous energy consumed. The greater this parameter, the greater the moment exerted on the wing and the more the energy consumed. Figure 7d shows that at the downstoke interval around $t/T = 0.25 \sim 0.75$, the absolute value of the bending moment is greater than that at the upstroke interval, which indicates that more energy is consumed during the downstroke interval for bird flight.

In Fig. 8, the labels are the nondimensional pressure, which is achieved by dividing pressure by double freestream dynamic pressure. The following features can be observed from Fig. 8:

1) At $t = 0.00T$, the wing is at the middle of the upstroke. In the case of the rigid wing, a high-pressure region occurs on the top surface of the wing, and a low-pressure region occurs on the bottom surface of the wing. Whereas, in the case of the doubly hinged wing, the pressure on the top surface of the doubly hinged wing is lower than the rigid wing.

2) At $t = 0.25T$, it is at the beginning of the downstroke. The rigid wing and the inner wing of the doubly hinged wing are stationary. Whereas, the outer wing of the doubly hinged wing continues to move upward. Thus, there is a high-pressure region on the top surface of the outer wing.

3) At $t = 0.50T$, it is at the middle of the downstroke. In the case of the rigid wing, the pressure contour is similar as that at $t = 0.0T$, but the high-pressure region is on the bottom surface. In the case of the doubly hinged wing, the pressure is close between the top and bottom surface.

4) At $t = 0.75T$, it is at the beginning of the upstroke. The rigid wing and the inner wing of the doubly hinged wing are stationary. The outer wing of the doubly hinged wing still moves downward. As can be seen, a low-pressure region occurs on the top surface of the outer wing.

Figures 9a–9c compare the moment components in Eq. (17) that determine the angular acceleration of the outer wing. Figure 9a shows that when $k_2 = k_1$, because the upward and downward deflection motions of the outer wing are symmetrical in the flapping cycle, the values of the moment components are correspondingly symmetrical. It was also found that when $k_2 = k_1$, the acceleration part of the moment of the inertial force about axis BD, M'_{α_1}, plays an important role in determining the angular acceleration of the outer wing. The velocity part of the moment of the inertial force about axis BD, M'_{ω_1}, is almost zero and is the weakest among the four moment components. Comparing Figs. 9a–9c, we found that when the elastic constant of the membrane on the lower surface is increased, the time interval as the outer wing deflects upward becomes less, and in this interval the elastic moment part M'_E and the aerodynamic moment part M'_{air} becomes greater. From Fig. 9, it was found that the value of

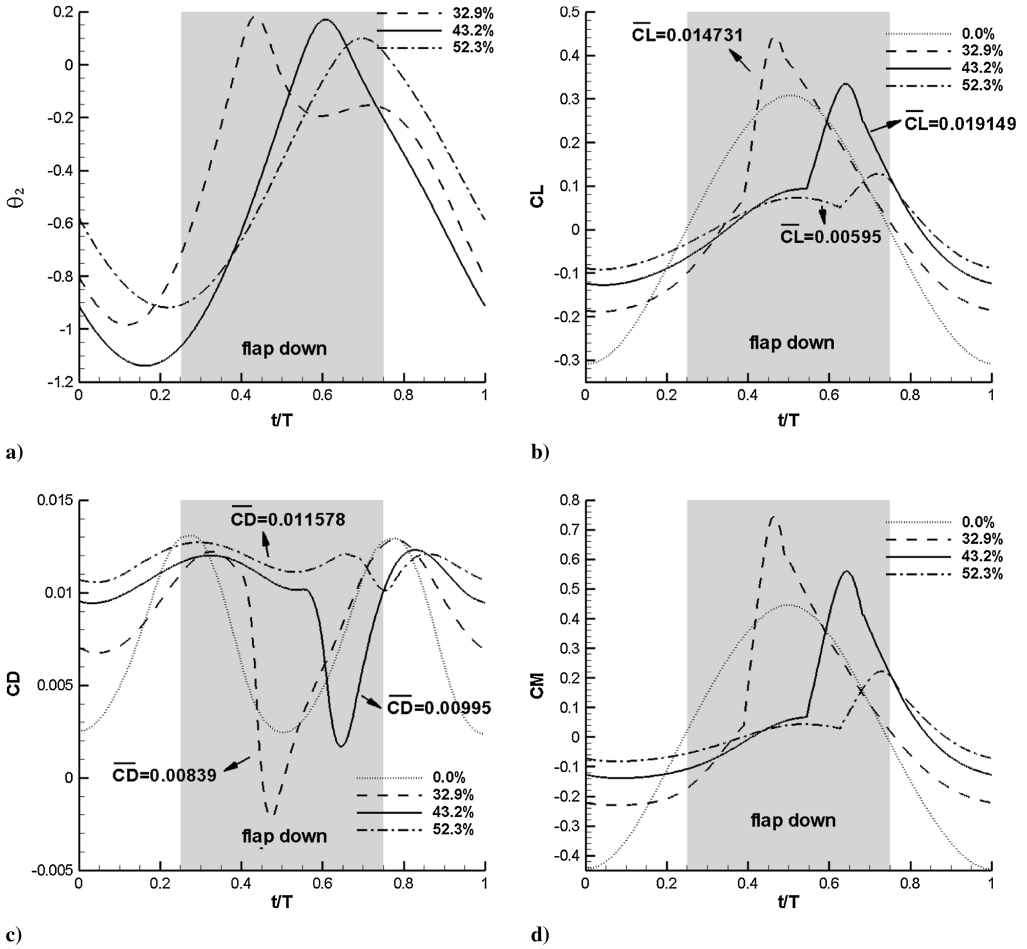

Fig. 10 Comparisons of doubly hinged wing for different hinge-axis positions, $k_2 = 50k_1$: a) the deflection angle of the outer wing as a function of time, b) the instantaneous lift coefficient as a function of time, c) the instantaneous drag coefficient as a function of time, and d) the instantaneous bending-moment coefficient about the wing root as a function of time.

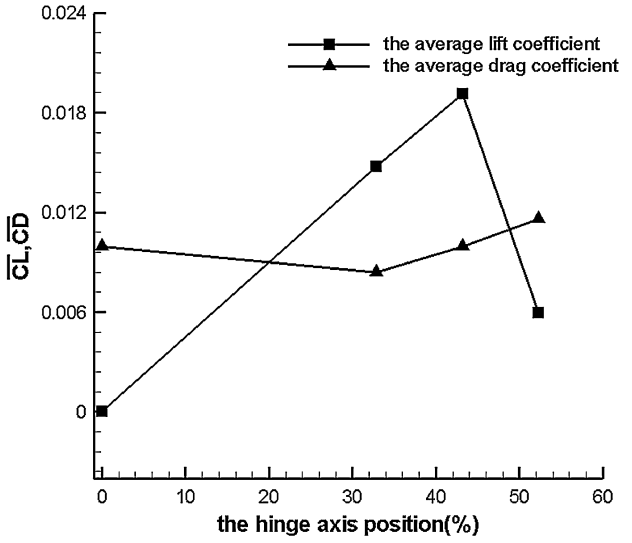

Fig. 11 Average lift and drag coefficients as a function of the hinge-axis position.

the velocity moment part M'_{ω_1} induced by the inertial force is always very small.

C. Effect of the Hinge-Axis Position

In this section, the aerodynamics for three different hinge-axis positions is simulated numerically. The parameters are listed in Table 1, and the elastic constant of the membrane on the lower surface is $k_2 = 50k_1$. First, two special cases are considered. The first case is that the hinge-axis position is 0.0% (i.e., the hinge axis approaches the outer wing tip infinitely). In this case, the outer wing is infinitely small, which corresponds to the rigid wing. The second case is that the hinge-axis position is 100% (i.e., the hinge axis approaches the inner root). In this case, the inner wing is infinitely small and the movement amplitude of the wing tip of the inner wing BD is infinitely small, and so the outer wing is in the state of rest. For these two special cases, the average lift should be zero. The drag for the first case should be very small, but the drag for the second case should be great, as the wing is stationary.

Next are the computational results. Figure 10 shows comparisons of doubly hinged wing for different hinge-axis positions, Fig. 11 indicates average lift and drag coefficients as a function of the hinge-axis position, and Fig. 12 shows comparisons of the moment components in Eq. (17) hat determine the angular acceleration of the outer wing. Figure 10a is the comparison of the deflection angle of the outer wing for three different hinge-axis positions. Figures 10b–10d are the instantaneous lift coefficient, instantaneous drag coefficient, and instantaneous bending moment about the wing root, respectively. It is seen from Fig. 10a that the inner wing flaps downward while the outer wing deflects upward. When the hinge axis moves from wing tip to root, the upward deflection interval of the outer wing moves backward in the flapping cycle, and the amplitude of the deflection angle becomes less. The maximum upward deflection of the outer wing for the 32.9, 43.2, and 52.3% cases is at about $0.45T$, $0.6T$, and $0.7T$, respectively. In Fig. 10a, two convex peaks appear on the deflection angle of the 32.9% case, whereas only one convex peak appears for other two cases. To interpret this phenomenon, Fig. 12 shows the comparisons of the moment components in Eq. (17) that determine the angular acceleration of the outer wing. The map name "total" in Fig. 12 means the summation of the four moment components in Eq. (17), whose value is multiple of α_2. Because $\alpha_2 = \theta''_2$, the sign of α_2 can determine the characteristic of the deflection-angle curve. From higher mathematics, it is known that when $\alpha_2 > 0$ in some definition range the curve of θ_2 is concave curve, and when $\alpha_2 < 0$ in some definition range the curve of θ_2 is convex curve. It is seen from Fig. 12 that the sign of α_2 for the 32.9% case is $+, -, +, -$, and $+$ in a flapping cycle, and the sign of α_2 for the 52.3% case is $+$, $-$, and $+$ in a flapping cycle. Thus, two convex peaks appear on the deflection-angle curve of the 32.9% case, whereas only one convex peak appears for the other two cases. From Fig. 12a, the sign of α_2 for the 32.9% case is $+$ at $t/T = 0.5$–0.6. This is because M'_{air} for the 32.9% case is so great.

It is seen from Figs. 10b–10d that the peak value of the curves is the greatest for the 32.9% case. This can be explained as follows. The outer wing deflects upward for the 32.9 and 43.2% cases when the inner wing is almost in the mid-downstroke period ($t/T = 0.5$), but the interval when the outer wing deflects upward for the 52.3% case is almost at the end of the downstroke. When the inner wing is in the mid-downstroke period the angular velocity of the inner wing is the biggest, and when the inner wing is in the period of the end of downstroke the angular velocity of the inner wing is almost zero. Because of these reasons, the peak value of the curves is the greatest for the 32.9% case, but is smallest for the 52.3% case.

Figure 11 is the average force coefficient as a function of different hinge-axis positions. The figure shows that when the hinge axis moves from the wing tip to the root, the average lift coefficient increases first, and then decreases, whereas the average drag acts in an opposite way. Figure 12 is a comparison of the moment components in Eq. (17) that determine the angular acceleration of the outer wing. Compared with the 52.3% case, the elastic moment part M'_E and the aerodynamic moment part M'_{air} for the 32.9% case are greater, but the acceleration part of the moment of the inertial force

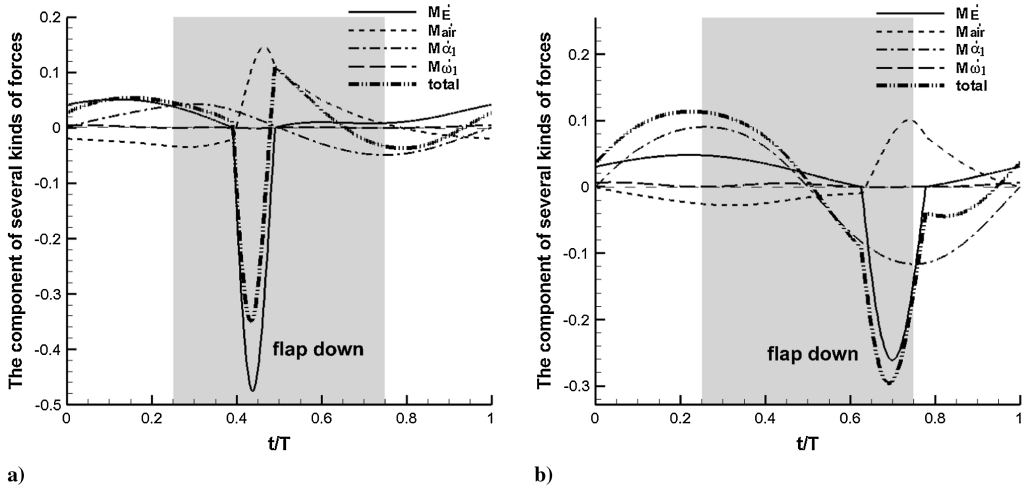

Fig. 12 Comparisons of the moment components in Eq. (17) hat determine the angular acceleration of the outer wing: a) the hinge-axis position (32.9%) and b) the hinge-axis position (52.3%). "Total" means the summation of the four moment components.

about axis BD (i.e., M'_{α_1}) is lower. The velocity parts of the moment of the inertial force about axis BD (i.e., M'_{ω_1}) for both cases are very small.

V. Conclusions

The mathematical model of the doubly hinged wing is established based on an existing patent. The deflection angle is determined by the aerodynamic, inertial, and elastic forces. The aero-elastic solver is composed of the N–S equations coupled to the wing dynamics. From a study of the effect of the elastic ratio k_2/k_1 and the hinge-axis position, the following conclusions were drawn:

1) When $k_2 > k_1$, the doubly hinged wing model can realize the nonsymmetrical deflection of the outer wing and simulate the bird wings' spanwise motion approximately. The doubly hinged wing model is shown to enhance the average lift coefficient compared to a rigid wing.

2) When increasing k_2/k_1, the time interval during which the outer wing deflects upward becomes shorter. The average lift coefficient increases with k_2/k_1 growing, but the rate of increase becomes smaller and smaller and tends to zero at the larger values of the elastic ratios considered. The average drag coefficient decreases first, and then increases as k_2/k_1 increases, suggesting an optimal k_2/k_1 for the maximized period-averaged lift-to-drag ratio.

3) When the hinge axis moves from wing tip to root, the average lift coefficient increases initially, and then decreases, but the average drag coefficient acts in an opposite way.

From these conclusions, the authors assert that the bird wing's spanning motion can enhance the lift effectively. The doubly hinged wing model in this paper can realize the spanning motion easily, thus may be used in the design of flapping micro-air vehicle (MAV). In the actual application, the ratio k_2/k_1 and the hinge-axis position should be selected to achieve the best aerodynamic performance. These conclusions should be meaningful to understand the mechanism of birds' flight and the design of MAVs.

Acknowledgments

Thanks to Faisal Amin and Qing Zhang for their help on the English grammar corrections. The authors also would like to thank the reviewers who helped improve the clarity of this paper.

References

[1] Shyy, W., Aono, H., Chimakurthi, S. K., Trizila, P., Kang, C.-K., Cesnik, C. E. S., and Liu, H., "Recent Progress in Flapping Wing Aerodynamics and Aeroelasticity," *Progress in Aerospace Sciences*, Vol. 46, No. 7, 2010, pp. 284–327. doi:10.1016/j.paerosci.2010.01.001

[2] Liu, P., and Bose, N., "Propulsive Performance from Oscillating Propulsors with Spanwise Flexibility," *Proceedings of the Royal Society of London, Series A: Mathematical, Physical and Engineering Sciences*, Vol. 453, No. 1963, 1997, pp. 1763–1770. doi:10.1098/rspa.1997.0095

[3] Zhu, Q., "Numerical Simulation of a Flapping Foil with Chordwise or Spanwise Flexibility," *AIAA Journal*, Vol. 45, No. 10, 2007, pp. 2448–2457. doi:10.2514/1.28565

[4] Heathcote, S., Wang, Z., and Gursul, I., "Effect of Spanwise Flexibility on Flapping Wing Propulsion," *Journal of Fluid Structures*, Vol. 24, No. 2, 2008, pp. 183–199. doi:10.1016/j.jfluidstructs.2007.08.003

[5] Chimakurthi, S. K., Tang, J., Palacios, R., Cesnik, C. E. S., and Shyy, W., "Computational Aeroelasticity Framework for Analyzing Flapping Wing Micro Air Vehicles," *AIAA Journal*, Vol. 47, No. 8, 2009, pp. 1865–1878. doi:10.2514/1.38845

[6] Aono, H., Chimakurthi, S. K., Cesnik, C. E. S., Liu, H., and Shyy, W., "Computational Modeling of Spanwise Flexibility Effects on Flapping Wing Aerodynamics," AIAA Paper 2009-1270, Jan. 2009.

[7] Viieru, D., Tang, J., Lian, Y. S., Liu, H., and Shyy, W., "Flapping and Flexible Wing Aerodynamics of Low Reynolds Number Flight Vehicles," AIAA Paper 2006-503, Jan. 2006.

[8] Shyy, W., Lian, Y. S., Tang, J., Viieru, D., and Liu, H., *Aerodynamics of Low Reynolds Number Flyers*, Cambridge Univ. Press, New York, 2008, pp. 10–11.

[9] Azuma, A., *The Biokinetics of Flying and Swimming*, 2nd ed., AIAA Education Series, AIAA, New York, 2006, pp. 149–156.

[10] Zeng, R., "Aerodynamic Characteristics of Flapping-Wing MAV Simulating Bird Flight," Ph.D. Dissertation, Nanjing Univ. of Aeronautics and Astronautics, Nanjing, PRC, Sept. 2004 (in Chinese).

[11] Lighthill, S. J., "The Inaugural Goldstein Memorial Lecture—Some Challenging New Applications for Basic Mathematical Methods in the Mechanics of Fluids that Were Originally Pursued with Aeronautical Aims," *Aeronautical Journal*, Vol. 41, No. 52, 1990, pp. 41–52.

[12] Lighthill, S. J., "Aerodynamics Aspects of Animal Flight," *Swimming and Flying in Nature*, edited by T. Y. Wu, C. J. Brokaw, and C. Brennen, Plenum, New York, 1975, pp. 423–491.

[13] Sato, M., "Analyses of Wing Motion Observed in the Flight of Living Creatures," Master's Thesis, Dept. of Engineering, Univ. of Tokyo, Tokyo, March 1980 (in Japanese).

[14] Toomey, J., and Eldredge, J. D., "Numerical and Experimental Study of the Fluid Dynamics of a Flapping Wing with Low Order Flexibility," *Physics of Fluids*, Vol. 20, No. 073603, 2008, pp. 1–10. doi:10.1063/1.2956372

[15] Vanella, M., Fitzgerald, T., Preidikman, S., Balaras, E., and Balachandran, B., "Influence of Flexibility on the Aerodynamic Performance of a Hovering Wing," *Journal of Experimental Biology*, Vol. 212, Jan. 2009, pp. 95–105. doi:10.1242/jeb.016428

[16] Ye, Z. Y., Wu, J., and Zhang, W. W., Patent for "A Flapping Equipment that Can be Used in Micro Air Vehicle," ZL200820028169.8, 2008 (in Chinese).

[17] Xie, F., "Numerical Simulation and Applications of Unsteady Flow in Low Mach Number," Ph.D. Dissertation, Northwestern Polytechnical Univ., Xi'an, PRC, June 2009 (in Chinese).

[18] Pletcher, R. H., and Chen, K.-H., "On Solving the Compressible Navier–Stokes Equations for Unsteady Flows at Very Low Mach Numbers," AIAA Paper 93-3368, July 1993.

[19] Dailey, L. D., and Pletcher, R. H., "Evaluation of Multigrid Acceleration for Preconditioned Time-Accurate Navier–Stokes Algorithms," AIAA Paper 95-1668-CP, 1995.

[20] Turkel, E., Radespiel, R., and Kroll, N., "Assessment of Preconditioning Methods for Multidimensional Aerodynamics," *Computers and Fluids Journal*, Vol. 26, No. 6, 1997, pp. 613–634. doi:10.1016/S0045-7930(97)00013-3

[21] Jameson, A., "Time Dependent Calculations Using Multigrid, with Applications to Unsteady Flows Past Airfoils and Wings," AIAA Paper 91-1596, 1991.

[22] Arnone, A., Liou, M. S., and Povinelli, L. A., "Integration of Navier–Stokes Equations Using Dual Time Stepping and a Multigrid Method," *AIAA Journal*, Vol. 33, No. 6, 1995, pp. 985–990. doi:10.2514/3.12518

[23] Rumsey, C. L., Sanetrik, M. D., Biedron, R. T., Melson, N. D., and Parlette, E. B., "Efficiency and Accuracy of Time-Accurate Turbulent Navier–Stokes Computations," AIAA Paper 95-1835-CP, 1995.

[24] Jameson, A., Schmidt, W., and Turkel, E., "Numerical Solution of the Euler Equations by Finite Volume Methods Using Runge–Kutta Time Stepping Schemes," AIAA Paper 81-1259, June 1981.

[25] Swanson, R. C., and Turkel, E., "Artificial Dissipation and Central Difference Schemes for the Euler and Navier–Stokes Equations," AIAA Paper 87-1107, June 1987.

[26] Swanson, R. C., and Turkel, E., "Multistage Schemes with Multigrid for Euler and Navier–Stokes Equations," NASA Langley Technical Report Server, 1997.

[27] Jameson, A., and Yoon, S., "Lower–Upper Implicit Schemes with Multiple Grids for the Euler Equations," *AIAA Journal*, Vol. 25, No. 7, July 1987, pp. 929–935. doi:10.2514/3.9724

[28] Yoon, S., and Jameson, A., "Lower–Upper Symmetric Gauss–Seidel Method for the Euler and Navier–Stokes Equations," *AIAA Journal*, Vol. 26, No. 9, Sept. 1988, pp. 1025–3026. doi:10.2514/3.10007

[29] Grasso, F., and Marini, M., "LU Implicit TVD Scheme for the Solution of Viscous Two Dimensional High Speed Flows," AIAA Paper 91-1573, June 1991.

[30] Menter, F., "Zonal Two Equation κ-ω Turbulence Models for Aerodynamic Flows," AIAA Paper 93-2906, July 1993.

[31] Menter, F., "Two-Equation Eddy-Viscosity Turbulence Models for Engineering Applications," *AIAA Journal*, Vol. 32, No. 8, Aug. 1994, pp. 1598–1605. doi:10.2514/3.12149

[32] Koochesfahani, M. M., "Vortical Patterns in the Wake of an Oscillating

Airfoil," *AIAA Journal*, Vol. 27, No. 9, 1989, pp. 1200–1205. doi:10.2514/3.10246

[33] Ramamurti, R., and Sandberg, W., "Simulation of Flow About Flapping Airfoils Using Finite Element Incompressible Flow Solver," *AIAA Journal*, Vol. 39, No. 2, 2001, pp. 253–260. doi:10.2514/2.1320

[34] Young, J., and Lai, J. C. S., "Oscillation Frequency and Amplitude Effects on the Wake of a Plunging Airfoil," *AIAA Journal*, Vol. 42, No. 10, 2004, pp. 2042–2052. doi:10.2514/1.5070

[35] He, X. S., Zhang, J. F., and Gao, X. S., *Theoretical Mechanics (I)*, Science Press, Peking, PRC, 2005, pp. 288–289 (in Chinese).

[36] Gordon, W. J., and Hall, C. A., "Transfinite Element Methods: Blending-Function Interpolation over Arbitrary Curved Element Domains," *Numerische Mathematik*, Vol. 21, No. 2, 1973, pp. 109–129. doi:10.1007/BF01436298

[37] Rizzi, A., and Eriksson, L. E., "Transfinite Mesh Generation and Damped Euler Equation Algorithm," AIAA Paper 81-0999, 1981.

[38] Tobalske, B. W., and Dial, P. K., "Flight Kinematics of Black-Billed Magpies and Pigeons Over a Wide Range of Speeds," *Journal of Experimental Biology*, Vol. 199, 1996, pp. 263–280.

C. Cesnik
Associate Editor